Journal of the European Ceramic Society 45 (2025) 117482

Contents lists available at ScienceDirect

Journal of the European Ceramic Society

journal homepage: www.elsevier.com/locate/jeurceramsoc

In situ compression of ceramic-organic supraparticles: Deformation and fracture behavior

Cong Yan [a], Alexander Plunkett [b,c], Büsra Bor [b], Erica Lilleodden [d,e], Gerold A. Schneider [b], Diletta Giuntini [a,b,*]

[a] Department of Mechanical Engineering, Eindhoven University of Technology, De Rondom 70, Eindhoven 5612 AP, the Netherlands
[b] Institute of Advanced Ceramics, Hamburg University of Technology, Denickestrasse 15, Hamburg 21073, Germany
[c] Tenneco Inc., Glinder Weg 1, Glinde 21509, Germany
[d] Helmholtz-Zentrum Hereon, Institute of Materials Mechanics, Max-Planck-Strasse 1, Geesthacht 21502, Germany
[e] Fraunhofer Institute for Microstructure of Materials and Systems, Walter-Hülse-Strasse 1, Halle 06120, Germany

ARTICLE INFO

Keywords:
Supercrystals
Nanocomposites
Supraparticles
Compression
Fracture

ABSTRACT

Supercrystalline nanocomposites (SCNCs) feature intriguing functionalities and exceptional mechanical properties, but they are usually confronted with challenges when it comes to processing them in larger bulk form. One way to tackle this problem is a hierarchical approach, for which spherical SCNCs, i.e. supraparticles (SPs), are promising candidates as building blocks. Understanding the mechanical behavior of SPs is thus a key step towards the development of robust, multifunctional and macroscopic SCNCs. Hereby, in situ compression tests are performed on SPs with varying sizes and levels of crosslinking of their organic ligands. A size-dependent deformation and fracture behavior emerges. Plasticity occurs in larger SPs, while small ones exhibit brittle fracture. Surface stress and compaction affect the elastic modulus. Fracture initiation sites shift from the center of SPs to their equatorial belts with the decrease of SPs' size. The inverse scaling relationship between fracture strength and SPs' sizes is rationalized via Griffith theory.

1. Introduction

Within the vibrant field of nanocomposites [1], supercrystalline nanocomposites (SCNCs) stand out for their sophisticated architectures and functional properties [2,3]. SCNCs consist of inorganic nanoparticles (NPs) surface-functionalized by organic ligands, which are organized into periodic structures [2–4]. These long-range ordered structures are analogous to those of atomic crystals, but on a larger length scale [5]. This characteristic, together with their slower timescales in nucleation, growth and deformation mechanisms [6], makes SCNCs a versatile analogical model for phenomena such as phase transformations and interactions between materials defects [7,8]. Furthermore, thanks to their periodic nanostructures, the inherent NP-associated properties can be preserved even in self-assembled materials, and additional mesostructural collective properties can be fostered, with potential applications in battery electrodes, catalysts, optoelectronic and magnetic devices [3,9–14].

However, an often overlooked but fundamental requirement for SCNCs to be applied into devices is their mechanical robustness. Their mechanical behavior is in general poorly understood, although efforts start to be directed towards characterizing their strength, fracture toughness, fatigue and creep behavior [4,5,15–25]. Even though typically weak and brittle, it has been shown that SCNCs can be significantly strengthened via crosslinking of their organic ligands [5,16]. Nevertheless, producing robust and large-scale (with sizes above tens of μm) SCNCs remains a challenge [26] since defects such as voids and cracks occur at this scale, significantly deteriorating their mechanical properties.

A potential workaround against this limitation comes from bioinspiration, and in particular from natural mineral-rich ceramic-organic composites able to achieve outstanding combinations of mechanical properties thanks to hierarchical structures [27]. Here, mineral nano-building blocks are arranged into multiple, self-similar superstructures interfaced by thin, softer organic phases on each hierarchical level [12,28,29]. Supercrystalline μm-sized spherical particles, i.e. "supraparticles" (SPs) are promising candidates for building blocks for these kinds of bioinspired multiscale materials [26]. SPs can be produced with tunable size and morphology, and with a high yield [30–32].

---

* Corresponding author at: Department of Mechanical Engineering, Eindhoven University of Technology, De Rondom 70, Eindhoven 5612 AP, the Netherlands
E-mail address: d.giuntini@tue.nl (D. Giuntini).

https://doi.org/10.1016/j.jeurceramsoc.2025.117482
Received 22 September 2024; Received in revised form 16 April 2025; Accepted 24 April 2025

Understanding and modulating the mechanical properties of SPs, together with their deformation and failure behavior, become then crucial steps in paving the way towards macroscopic, robust and functional SCNCs.

Microcompression is a versatile technique to assess the mechanical response of spherical particles, particularly those in the μm range or even smaller. When subjected to compression with a flat punch, a variety of spherical particles has been tested to extract elastic response, sometimes plastic behavior, and fracture mechanisms [33–36]. The compression of spheres is particularly suited to identify the Young's modulus (E) and the transition from elastic to plastic deformation (yielding point) via Hertz theory [37–41]. On the other hand, in contrast to uniaxial deformation, compressing spherical particles induces a non-uniform stress state in the tested domain, with higher stress at the contact region, progressively decaying when moving away from the contact point [33,36,42]. To address this, the harmonic mean method has been introduced to describe stresses and strains in spherical particles [43]. Finite element methods are also extensively utilized [37,42]. The strength of spherical particles has also been investigated over the years by Hiramatsu and Oka, Shipway and Hutchings and recently by Pejchal et al. [44–48]. These studies reveal that the fracture initiation shifts from the spherical particles' center to their equatorial belt, where hoop stress can induce meridian cracks, and that their strength, determined from the peak of first principal stress either in the center or along the equator, correlates well with the transition of failure initiation sites [47,48].

Most of these studies, however, address "traditional" crystalline or amorphous particles, and not SPs, with one recent exception testing ligand-free colloidal SPs [49]. Previous works have nevertheless highlighted the crucial role of organic ligands in influencing the mechanical properties and the deformability of SCNCs [50], thus calling for investigations on the behavior of organic-inorganic SPs under compression.

In this study, the mechanical response of organic-inorganic SPs with varying sizes and degrees of organic crosslinking has been explored via in-situ microcompression in the scanning electron microscope (SEM). The harmonic mean method and fracture theories proposed for crystalline spherical particles are critically applied to SPs, i.e. assemblies of crystalline nanoparticles. Size-dependent phenomena are observed in the SPs with or without crosslinking, in terms of supercrystalline structure, deformation and fracture behavior. A size effect in the elastic modulus is rationalized through the influence of surface stress, while the Griffith theory is adopted for the size-dependent fracture strength.

2. Materials and methods

The SPs were prepared via emulsion templated self-assembly from a suspension of iron oxide NPs (Fe_3O_4, with a diameter of 15.2 ± 1.2 nm, from CAN GmbH, Germany) stabilized with oleic acid, as detailed in the previous work and summarized in SI section 1 [30]. The SPs are deposited on silicon substrates via dispersion in ethanol and spin coating. Some SPs were subjected to heat treatment (HT) at 325 ℃ under N_2 atmosphere (heating and cooling ramps of 1℃/min, holding time of 18 min) to induce the crosslinking of the oleic acid [5,16]. In some cases, squalene was added to the nanoparticle suspensions before self-assembly to produce SPs with an excess of organic ligands, with the aim of improving deformability by a reduced friction of single particles and/or added plasticity. The characteristics of all SPs tested in this study are provided in Table 1, including the degree of crosslinking, concentration of squalene and size. In the following, SPs are designated based on the presence or absence of heat treatment, together with their diameters (analyzed via *ImageJ* on pre-loading SEM micrographs). When present, the concentration of squalene will be specified.

The compression of SPs without squalene was carried out in-situ using a diamond flat punch ($D = 15$ μm) in a microcompression setup (KLA Tencor, formerly Nanomechanics, Inc.) in the Nova Nanolab 200 Dualbeam SEM/FIB (Thermofisher scientific, formerly FEI) at the Institute of Materials Mechanics of the Helmholtz-Zentrum Hereon, Geesthacht, while ex-situ tests were conducted in a G200 nanoindenter (Agilent, USA) for those with squalene. It is assumed that the electron beam has a negligible influence on the mechanical behavior of the SPs, as the Young's modulus determined from in situ microcompression aligns closely with that obtained ex situ for analogous materials [15,17]. A procedure involving 5 loading-holding-unloading cycles was adopted. First, the SPs were compressed to a targeted displacement to achieve ~2 % nominal strain (ratio of displacement to SPs' diameter) with constant displacement rate (10 nm/s, except for non-HT-15μm-SP, deformed at 50 nm/s), followed by a load-holding segment of 10 s. Subsequently, the load was released to 20 % of the previous maximum load, and then held for 10 s to stabilize the SPs before the next loading cycle. The details about the loading path for each SP is reported in SI Table S1. The procedure is repeated until fracture. The data recorded during the holding period under 20 % of the maximum load is utilized to eliminate thermal drift. All compression tests were checked in situ and post-mortem to make sure than only single SPs were tested, and not clusters of them. Data was excluded from the analysis once doubts emerged that multiple SPs were loaded simultaneously.

3. Results and discussion

3.1. SP structures

The uniform and nonporous SPs exhibit spherical geometry, as illustrated in Fig. 1(a) & (b), with an almost entirely supercrystalline structure. Notably, different supercrystalline packings are observed. Indeed, various structures have been observed in SPs, ranging from Mackay icosahedral symmetry to anti-Mackay rhombicosidodecahedral structures and single FCC (face-centered cubic) domains, with the increase in the size of SPs [51]. In Fig. 1(a), the small SP (diameter: ~ 534 nm, indicated by the white arrow) displays the anti-Mackay rhombicosidodecahedral structure, consisting of twelve pentagonal faces, twenty triangular faces and thirty rectangular faces [51]. In contrast, FCC packing is observed in a larger SP (diameter: ~680 nm), featuring the typical step edges due to spherical confinement, as depicted in Fig. 1(b). The transition of crystalline structure is related to the size of SPs because small SPs with icosahedral symmetry are more entropically favorable compared to the FCC structure [52,53]. A finite number of particles above 100 organizes into the icosahedral symmetry with either Mackay or anti-Mackay structure. They are then slowly architected into the single FCC domain if the number exceeds 2.5×10^4, where the nanostructure transitions displayed in Fig. 1(a) & (b) coincide with simulation results [54].

Table 1

Summary of SPs with different degrees of crosslinking, squalene concentrations and sizes.

	Squalene concentration (wt%)	Diameter (μm)						
HT	0	0.50	0.55	0.61	0.78	1.28	4.24	6.00
non-HT	0	3.00	3.60	7.20	15.00			
	1	0.89	2.73	3.41	3.46			
	2	2.57	4.26					
	5	1.57	2.93	3.68				

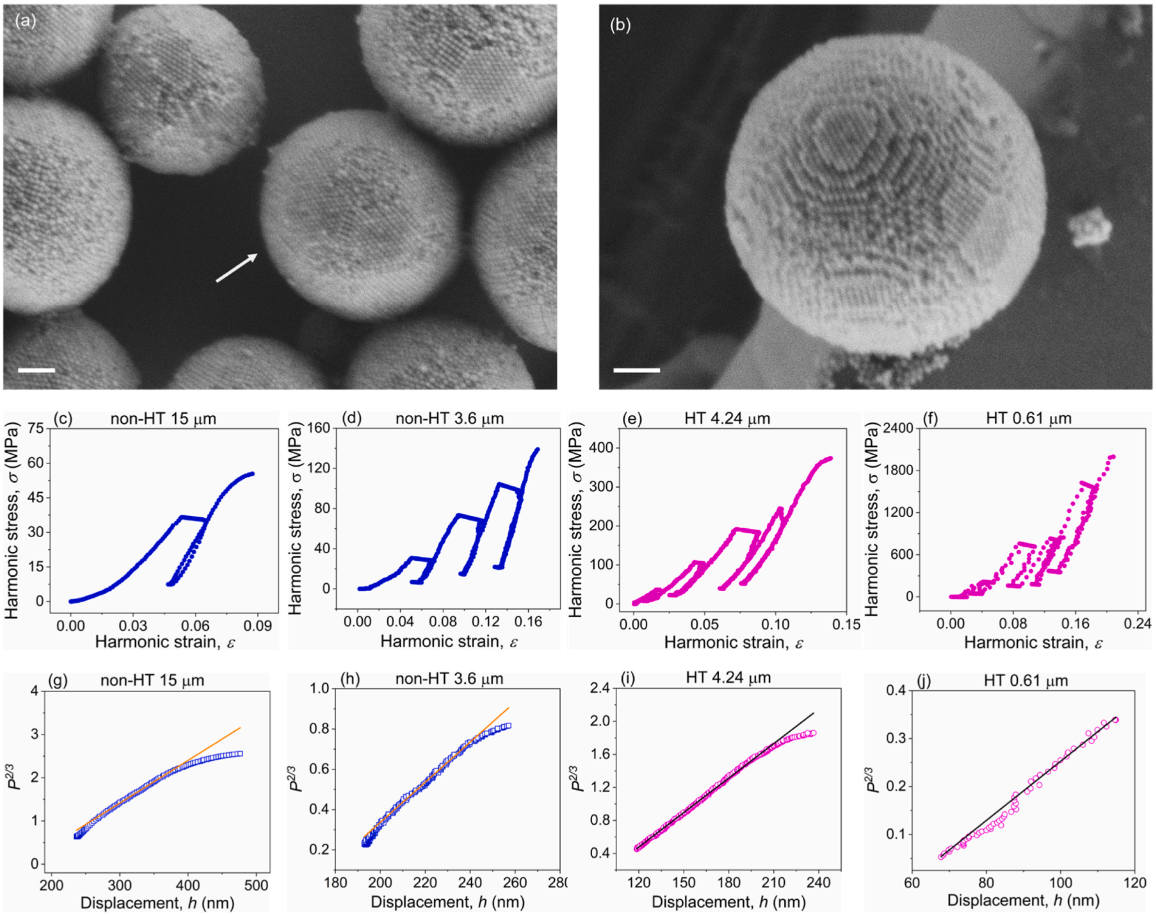

Fig. 1. Structure and deformation behavior of SPs. a) – b) SEM images of SPs showing different crystalline structures: a) SP with anti-Mackay rhombicosidodecahedral structure (indicated by the white arrow); b) SP with single FCC structure. Scale bars: 100 nm. c) – f) Harmonic stress-strain curves of representative SPs: c) non-HT 15 μm; d) non-HT 3.6 μm; e) HT 4.24 μm; f) HT 0.61 μm. g) – j) Identification of yielding point via Hertz theory for different SPs: g) non-HT 15 μm; h) non-HT 3.6 μm; i) HT 4.24 μm; j) HT 0.61 μm. The scatters in the plots are experimental data while solid lines refer to the Hertz model. One larger and one smaller SP are selected from both HT and non-HT SPs.

3.2. Stress and strain

The stress state of a sphere under compression is non-uniform, with distribution dependent on the relative loading contact radius with respect to the sphere's radius [47,48]. For a representation of equivalent stress and strain state in the SPs, the harmonic mean method is employed [43], aiming at avoiding biases in the stress and strain distribution.

At the contact region, high stresses are generated even under a small load, due to the localized contact area. The contact radius can be determined based on the geometrical relationship:

$$a_c = \left(Rh - \frac{h^2}{4}\right)^{0.5} \tag{1}$$

where a_c is the contact radius, R is the SP radius and h is total displacement divided to consider for the contact on the top and bottom of SPs. The contact stress is defined as

$$\sigma_c = \frac{P}{\pi {a_c}^2} \tag{2}$$

where σ_c is the contact stress and P is the measured load. The strain definition as proposed by Tabor is utilized [55], here considering the two contacts, top and bottom:

$$\varepsilon_c = 2 \bullet 0.2\left(\frac{a_c}{R}\right) \tag{3}$$

As for the region away from the contact, the SP is approximated to have a cylindrical shape to obtain the effective radius. The effective radius here (R_{eff}) is calculated based on volume conservation [43]:

$$R_{eff} = 1.155R\left(\frac{R}{2R - h}\right)^{0.5} \tag{4}$$

The resulting uniform stress and strain can then be calculated as:

$$\sigma_{cyl} = \frac{P}{\pi {R_{eff}}^2} \tag{5}$$

$$\varepsilon_{cyl} = \frac{h}{2R} \tag{6}$$

where σ_{cyl} and ε_{cyl} are the stress and strain in the cylinder, respectively.

Spheres under compression show a "sandwich" stress/strain distribution field, with high stresses/strains at the loading points, and lower, relatively uniform stresses/strains in-between. The harmonic mean method is utilized here to give a more representative description of their distribution within the overall SPs. This is a mathematical average approach that can mitigate the impact of large outliers, which is here considered appropriate to address the stress/strain distribution in SPs. The general definition is $H(x_1, \quad x_2, \quad \cdots, x_n) = \frac{1}{\frac{1}{n}\sum_{i=1}^{n}\frac{1}{x_i}} = \frac{n}{\sum_{i=1}^{n}\frac{1}{x_i}}$, and the harmonic mean stress can thus be obtained by considering the stress in the contact region (Eq. (2)) and that from cylinder assumption (Eq. (5)) as [43]:

$$\sigma_m = \frac{2}{\frac{1}{\sigma_c} + \frac{1}{\sigma_{cyl}}} \tag{7}$$

The harmonic mean strain can also be determined with the same approach as [43]:

$$\varepsilon_m = \frac{2}{\frac{1}{\varepsilon_c} + \frac{1}{\varepsilon_{cyl}}} \tag{8}$$

The harmonic stress-strain curves of four representative SPs, with and without crosslinking of the organic ligands, are shown in Fig. 1(c) – (f). The load-displacement and corresponding stress-strain curves of all SPs are shown in Fig. S3. The raw data was initially corrected to eliminate the impact of thermal drift, see SI section 3 for details. The last cycle of the harmonic stress strain curves shows some variations for the different SPs. The curve becomes more nonlinear as the SP diameter increases for non-HT SPs, together with a lower stress value at the nonlinearity onset. The harmonic stress-strain curve becomes slightly curved downward before fracture for the larger HT SP (diameter 4.24 μm, Fig. 1(e)) while no nonlinearity is visible with the SP's size reducing to 0.61 μm (Fig. 1(f)). This shows a size-dependent deformation behavior of SPs, which will be further analyzed later. We also observe that HT SPs (Fig. 1(e) & (f)) can sustain much higher stresses compared with their non-HT counterparts (Fig. 1(c) & (d)), confirming the enhanced mechanical properties induced by the organic crosslinking [15,16,18,19,22]. Note the extremely high stresses, up to 2 GPa sustained by the smaller HT SPs, but also the strengths $>$ 100 MPa reached by non-crosslinked SPs, which are still considerably high [49]. It is worth noting that the data becomes noisier for smaller SPs, due to the smaller displacements. A tendency of the SPs to creep can also be noticed in all stress-strain curves (Fig. S3), a phenomenon that has been previously reported for this materials system [19]. Hysteresis loops, another indication of viscous behavior, are also visible in larger non-HT SPs (Fig. 1(c)).

As mentioned in Materials and methods section, SPs with an excess of organic ligands (squalene) were also prepared, with the aim of achieving better deformability [50]. However, it results that cracks here appear earlier than in SPs without squalene, mostly during the first or second loading cycle. A typical harmonic stress-strain curve for squalene-enriched SPs, taken from a non-HT 2.57 μm SP with 2 wt% squalene, is displayed in Fig. 2, while all others are shown in Fig. S4. The respective harmonic strains at fracture are shown in Fig. S5, where it can be seen that SPs with squalene fail at smaller strains than the squalene-free ones. No clear trend on the effect of squalene concentration is observed. The overall lower mechanical properties of these SPs are likely associated with squalene creating defects due to phase separation or with poor interactions between squalene and oleic acid.

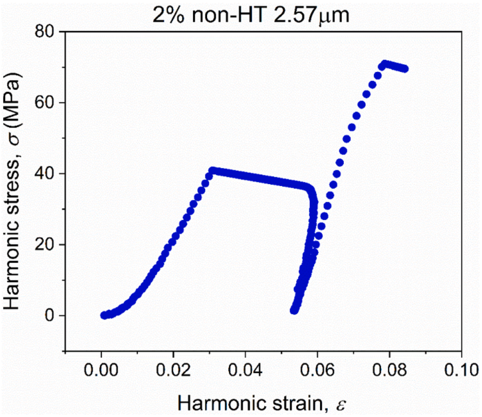

Fig. 2. Harmonic stress-strain curve of non-HT 2.57 μm SP with 2 % squalene.

3.3. Yield

The yielding point, indicating the emergence of plastic deformation, can be identified as the deviation from the linear regime in the uniaxial stress-strain curves [56]. However, a more accurate method to identify deviations from the elastic regime relies on the Hertz contact theory, already broadly applied in studies on compression of spherical particles [49].

The Hertz theory applies to two elastically contacting bodies, and the relationship between the load (P) and displacement (h) is expressed as [57]:

$$P = \frac{4}{3} \quad E_{eff} {R_{eff}}^{0.5} h^{1.5} \tag{9}$$

The effective Young's modulus (E_{eff}) is computed as:

$$\frac{1}{E_{eff}} = \frac{1-\nu_s^2}{E_s} + \frac{1-\nu_p^2}{E_p} \tag{10}$$

where the subscripts s and p denote sample and flat punch; E and ν are Young's modulus and Poisson's ratio, respectively. The effective radius (R_{eff}) can be calculated as:

$$\frac{1}{R_{eff}} = \frac{1}{R_s} + \quad \frac{1}{R_p} \tag{11}$$

where R_s and R_p denote the radius of SP and flat punch, respectively. The radius of the flat punch tends to infinity, so $R_{eff} = R_s$. Using Eqs. (9) – (11), the following relationship can be obtained:

$$P^{2/3} = c * h \tag{12}$$

where c is dependent on the effective modulus and SPs' radius.

Eq. (12) is then applied to the last loading step of compression tests, where the nonlinearity occurs, as depicted in Fig. 1(g) – (j). Significant deviations between the Hertz contact model and experimental data can be noticed in non-HT 15 and 3.6 μm SPS, and in HT 4.24 μm SP, while a good alignment between the two is found in HT 0.61 μm SP, implying that plasticity occurs in the former, but the smaller crosslinked SP exhibits brittle fracture, i.e. with no occurrence of plastic deformation before failure. With the same approach, plastic deformation is also verified in HT 1.28 μm SP (Fig. S6), whereas all other SPs (non-HT 3 μm and HT 0.78/0.55 μm SPs) fracture in a brittle manner.

The plastic deformation in SPs can be ascribed to the mediation of organic ligands facilitating the movement of NPs because no signal of yielding has been observed in NPs in previous works on the compression of supercrystalline micropillars [50,58]. The good match between Hertz model and experimental data in the earlier loading steps of compression tests implies that plasticity only emerges in the last step. The accumulated deformation is likely to originate from the creep behavior illustrated in Fig. S3, since creep deformation takes time to recover, as reported in the previous study [19]. Fig. 1(c) – (j), Fig. S3 and Fig. S6 point out a transition in the deformation behavior - from brittle fracture (without plasticity) to fracture with minor plasticity (harmonic plastic strain: 0.005 $\sim$ 0.02) with the increase in SPs' sizes. Furthermore, the verification of whether the deviation from the linear regime on the harmonic stress-strain curves can imply the occurrence of plasticity is conducted with the Hertz contact model as benchmark, see details in SI section 8. The two approaches give comparable results, indicating that the curvature of harmonic stress-strain curves also indicate the emergence of yield.

3.4. Stiffness and compaction

The influence of multiple loading cycles on the mechanical behavior of SPs, and in particular on their Young's modulus, is explored by shifting the origin of all load-displacement curves to zero, as illustrated for four representative SPs in Fig. 3. One can observe that the curves become steeper at each loading cycle, and that this trend becomes less marked with increasing cycle numbers, irrespective of the presence of crosslinking. Steeper curves indicate that the SPs become stiffer as the compression tests proceed. We attribute this stiffening to the compaction of SPs, a consequence of the "squeezing" of organic ligands in the inter-NP spacings and into superlattice's interstitial sites, as previously observed under indents in the same material system [15,50]. The stiffening is less marked in HT SPs, since in those systems the crosslinking immobilizes the organic ligands and thus hampers their compaction. Although the hydrostatic stress component under uniaxial compression conditions is not as pronounced as in indentation tests [39], its effect on the compaction of organic ligands should not be overlooked. Ongoing

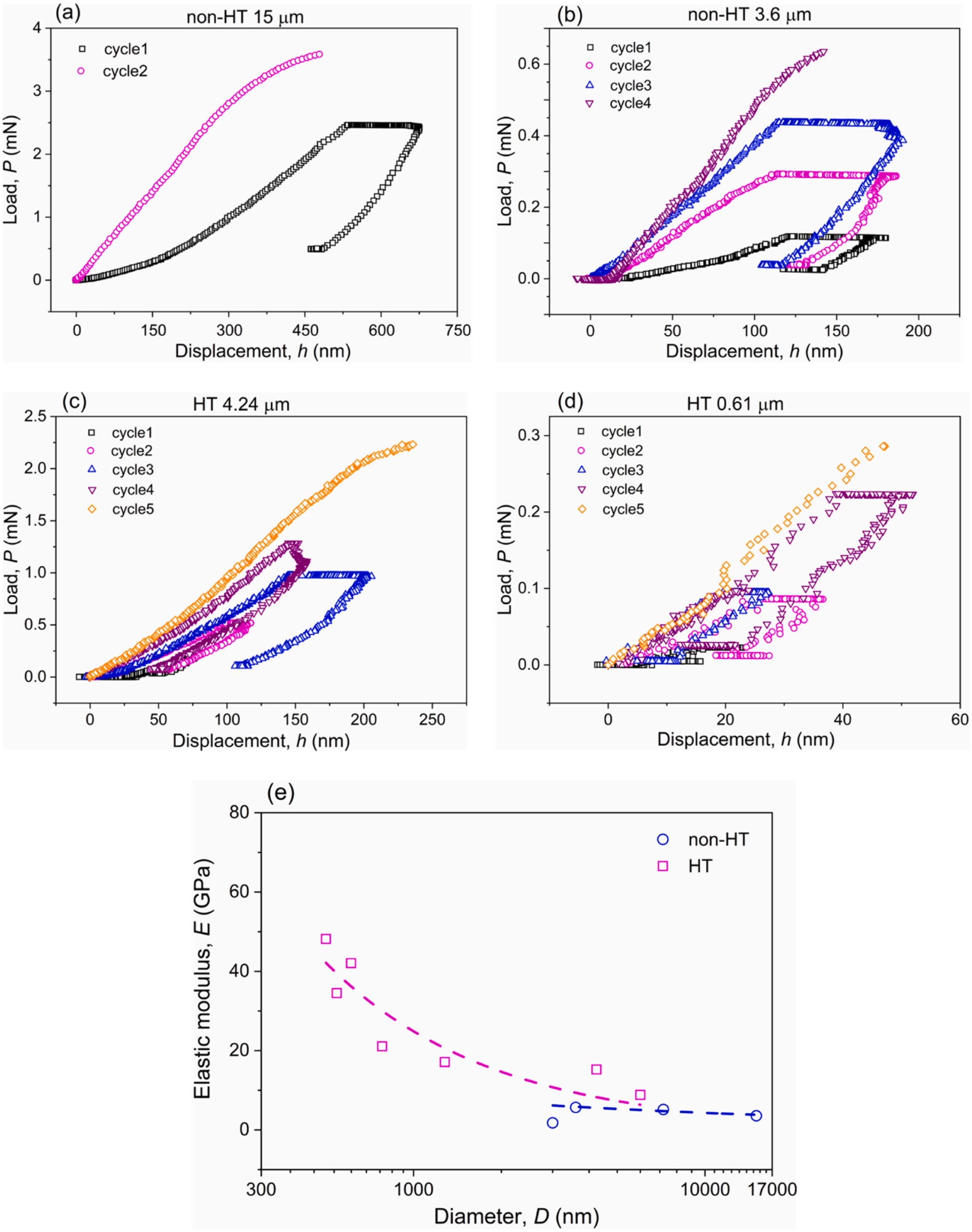

Fig. 3. Analysis of compaction and elastic modulus of SPs. a) – d) Load-displacement (*P*-*h*) curves of different SPs with all loading cycles shifted to zero: a) non-HT 15 μm; b) non-HT 3.6 μm. c) HT 4.24 μm; b) HT 0.61 μm. e) Elastic modulus of SPs with varying sizes.

work in our same group is indeed demonstrating the existence of free volume in SCNCs, likely located in the sub-nm spacings between NPs where organic ligands are confined and in the tetrahedral and octahedral interstitial sites of FCC superlattices [59]. The free volume provides available space for the compaction of organic ligands, resulting in stiffer SPs as compression tests progress.

The elastic modulus of SPs is determined again with the Hertz contact model, taking the two different contacts into consideration: 1) on the top – between the diamond flat punch and the SPs; 2) on the bottom – between SPs and the silicon substrate they sit on. The corresponding reduced moduli can be expressed as [60]:

$$\frac{1}{E_{top}}=\frac{1-{\nu_s}^2}{E_s}+\frac{1-{\nu_p}^2}{E_p} \tag{13}$$

$$\frac{1}{E_{bottom}}=\frac{1-{\nu_s}^2}{E_s}+\frac{1-{\nu_{sub}}^2}{E_{sub}} \tag{14}$$

where E_{top} and E_{bottom} are the reduced moduli of contacts on the top and bottom, respectively. The subscripts s, p and sub denote SPs, flat punch and substrate, respectively.

The effective modulus in Eq. (9) is then expressed as the average of E_{top} and E_{bottom}:

$$E_{eff}=\frac{E_{top}+E_{bottom}}{2} \tag{15}$$

With Eq. (9) & Eqs. (11) – (15), the apparent Young's modulus of SPs is determined from the loading phase of each test, and is displayed in Fig. 3(e). The data from cycle 1 is utilized to obtain the moduli, to meet the assumptions of Hertz theory (i.e. elastic deformation regime) and minimize the effect of compaction. HT SPs exhibit higher apparent elastic stiffness compared to their non-HT counterparts, again due to crosslinking of organic ligands [16,19]. The apparent elastic modulus consistently drops with increasing SP size, regardless of crosslinking, indicating a size-dependent elastic modulus.

Size effect in Young's modulus have been widely reported in nanospheres and nanowires consisting of various material categories, for which this effect is commonly attributed to the surface effect where the surface stress play a dominating role [41]. Surface stress refers to the reversible work per unit area required to elastically stretch a preexisting surface [61,62]. The work applied during the compression of SPs can thus be divided into two components: the work used to stretch the surface of SPs to accommodate the change in the geometry and that to compress the inner core of SPs (see details in SI Section 9).

The correlation between the apparent elastic modulus of SPs and their sizes can be ultimately determined as: $E_{app} \sim E_b+g\bullet\frac{\tau_s}{D}$, where E_{app} and E_b are the apparent and bulk elastic moduli of SPs, g is a coefficient that scales with ε^{-2} (ε is the strain of SPs), τ_s is the surface stress and D is the SPs' diameter. τ_s is reported to be in the range of $1\sim10$ N/m for several materials [61,62] and it is reasonable to assume its value for SPs to be of the same order of magnitude. The strain of SPs during the 1st loading cycle is typically a few percent (1–5 %, see Fig. 1(c-f)), dependent on the sizes of SPs. Consequently, g is estimated to be around 10^3-10^4. The 2nd term in the above formula, representing the influence of surface stress, can lead to an increase of the apparent elastic modulus by tens of GPa, aligning well with the results shown in Fig. 3(e). The coordination of NPs, as well as the bonding of organic ligands on the surface of SPs differs from those in the core, resulting in a smaller interparticle distance for the NPs on the surface and thus applying the compressive stress to the core of SPs. The overall SP surface to volume ratio increases with reducing SP size, amplifying the surface effect on the mechanical properties of entire SPs. Consequently, an increase in elastic modulus is observed as the SPs become smaller, in particular for those with the diameter smaller than 1 μm. Another factor that could be contributing to this size effect for E is the potential presence of a core-shell structure in the SPs. This has however not been observed in our system, and can be the object of future work.

Apart from surface stress, compressive stress has been recognized as another factor contributing to the enhancement of the elastic modulus of silicon and titanium spheres (by decreasing the distance between nearest neighbors) [39]. Even in the first loading cycle, some compaction effect will still be present. Higher stresses are usually induced in smaller SPs (Fig. 1), suggesting more pronounced compaction in these cases. The compressive stress effect can then further contribute to the arising of a size-dependent elastic modulus.

Note that the strain rates during the compression of SPs vary with their sizes, increasing as the SPs become smaller. This difference can reach up to one order of magnitude between HT 6 μm SP (largest) and HT 0.5 μm SP (smallest). However, its contribution to the elastic stiffening of organic ligands is estimated to be up to ~ 12 % among all the SPs explored here, an effect that further becomes more negligible if one considers the overall SPs (see details in SI section 10).

3.5. Fracture

Even though some plasticity is observed in larger SPs, most of them fail in a brittle manner, prompting an analysis of their fracture behavior. The key parameter for failure of brittle elastic spherical particles is the first principal stress field [47,48,63]. The location of the peak of first principal stress, considered as the fracture stress, is highly sensitive to the relative contact radius a_c/R (where a_c is the contact radius and R is the spherical particle's radius), shifting from the contact perimeter (a_c/R < 0.3) to the sphere's center ($0.3 < a_c/R < 0.65$) and then to the equator ($a_c/R < 0.65$) [47]. Since here no SP fails with a_c/R below 0.3, we are only interested in the first principal stress in the SPs' center and along their equatorial belt, which can be expressed as [48]:

$$\sigma_{1c}=\frac{P}{\pi R^2}\bullet\widetilde{\sigma}_{1c}\left(\frac{a_c}{R},\nu,\mu\right) \tag{16}$$

$$\sigma_{1e}=\frac{P}{\pi R^2}\bullet\widetilde{\sigma}_{1e}\left(\frac{a_c}{R},\nu,\mu\right) \tag{17}$$

where subscripts c and e denote the center and equator, respectively, P is the compressive load applied to the SPs, $\widetilde{\sigma}_{1c}$ and $\widetilde{\sigma}_{1e}$ are the normalized first principal stress in the center and equatorial belt, which are functions of relative contact radius (a_c/R), Poisson's ratio (ν) of SPs and friction coefficient (μ) at the flat punch-SPs contact. By means of the finite element method, 5th order polynomial expressions of $\widetilde{\sigma}_{1c}$ and $\widetilde{\sigma}_{1s}$ have been calculated as [63]:

$$\widetilde{\sigma}_{1c}\left(\frac{a}{R},\nu,\mu\right)=\sum_{i=0}^{5}c_i(\nu,\mu)(a_c/R)^i \tag{18}$$

$$\widetilde{\sigma}_{1e}\left(\frac{a}{R},\nu,\mu\right)=\sum_{i=0}^{5}e_i(\nu,\mu)(a_c/R)^i \tag{19}$$

respectively, where c_i and e_i are the corresponding coefficients. The Poisson's ratio has previously determined as 0.34 for the same material system (in crosslinked state) using the finite element method and this value is here used for both crosslinked and non-crosslinked SPs [64]. The friction coefficient at the contact is taken as 0.05. Utilizing bi-linear interpolation [63], the coefficients in Eq. (18) & (19), i.e. c_i and e_i, given $\nu = 0.34$ & $\mu = 0.05$, can be determined (see Table 2).

By using Eq. (18) & (19) with the corresponding coefficients in Table 2, the normalized first principal stress in the center ($\widetilde{\sigma}_{1c}$) and

Table 2
Values of coefficients: c_i and e_i in Eqs. 18 and 19.

i	0	1	2	3	4	5
c_i	0.61	−0.03	−0.17	−1.65	2.17	−1.24
e_i	0.45	−0.05	0.32	−1.25	1.73	−0.97

equatorial belt ($\widetilde{\sigma}_{1e}$) can be calculated, as plotted in Fig. 4(a). The corresponding stresses at failure for all SPs as a function of their diameter is shown in Fig. 4(b). Consistent with previous observations, the peak of the first principal stress is located in the center of SPs for small contact areas, and then shifts to the equatorial belt as a_c/R increases. The shift emerges when a_c/R reaches ~ 0.5, which is smaller than the previously reported value (calculated for $\nu = 0.17$) due to the dependence on the material's Poisson's ratio [47]. Additionally, the first principal stress in the SP center sharply decreases, while that along the equator exhibits a mild drop with rising a_c/R.

The shift of first principal stress peak leads to a transition in the sites of failure initiation. In Fig. 4(c), larger SPs typically fail with a low value of a_c/R while smaller SPs exhibit the opposite phenomenon. After examining their morphologies post-fracture, a transition of failure initiation sites becomes apparent, as illustrated in the SEM images in Fig. 4(c). For larger SPs, plotted in the region with a light green color, the failure onset is at the center of SPs, which ultimately break into many small fragments. Distinct morphologies are observed for smaller SPs, as plotted in the grey-colored region. In this case, SPs break into only several relatively large pieces resulting from meridian cracks (indicated by the yellow dashed line), which originate from hoop stresses along the equatorial belt. The transition of initiation sites of failure, from the center of SPs to the equatorial belt with decreasing SP size, can be attributed to the shift of peak of first principal stress. These experimental observations coincide with the model's prediction shown in Fig. 4(a).

In Fig. 4(b), smaller SPs display higher fracture stress (peak of first principal stress) whereas the opposite is observed for larger ones, regardless of crosslinking, revealing a size-dependent fracture strength. This trend becomes more pronounced for HT SPs. The Griffith fracture theory is employed here to explain the size-dependent fracture strength of SPs. The SEM images in Fig. 4(c) point out that the failure of SPs is caused by cracks, irrespective of the initiation from the center or equatorial belt. It should be mentioned that a certain level of crack deflection is commonly observed in the fractured SPs, and that this phenomenon coincides with previous works demonstrating that the organic ligands play a role toward extrinsic toughening in these kinds of supercrystals [15].

According to the Griffith criterion of fracture [56,65], the critical fracture stress (σ_c) is

$$\sigma_c = \sqrt{\frac{2E\gamma}{\pi a}} \bullet f \tag{20}$$

where E is the Young's modulus of SPs, f is the geometry factor, γ is the surface energy density and a is the size of the largest defect pre-existing in the SP. The parameter γ represents the energy required to break interactions between NPs in SPs, either dominated by van der Waals forces in non-crosslinked SPs or covalent bonds in crosslinked ones. For each SP category (crosslinked or not), γ is assumed to have the same value, since there is no difference in terms of the number of bonds and the binding energy in HT or non-HT SPs consisting of NPs of the same size and with the same functionalization. The parameter a refers to the size of

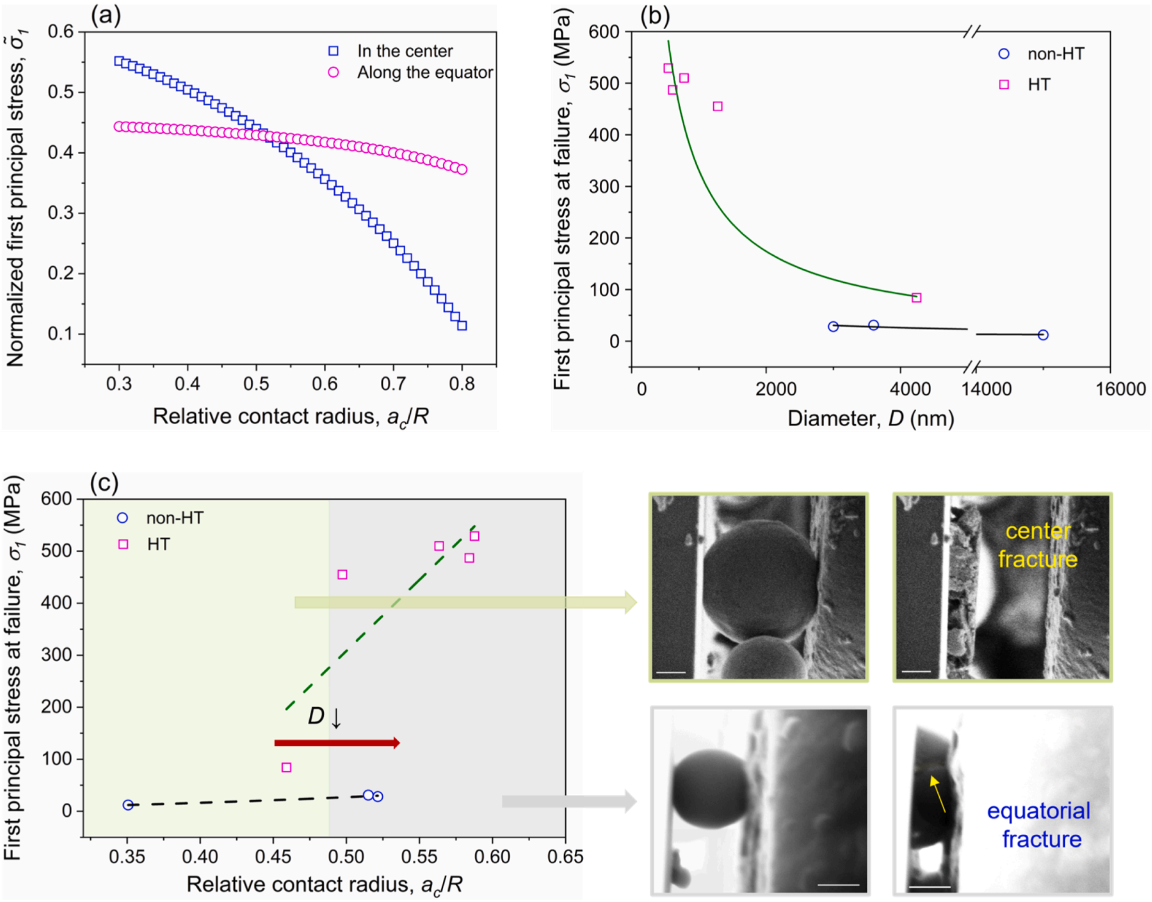

Fig. 4. Analysis of fracture behavior of SPs. a) Evolution of normalized first principal stress (in SPs' center and at the equator) with relative contact radius, revealing the peak of first principal stress shifting from the center to the equator as the compression progresses; b) The relationship between first principal stress at failure and SPs' diameters, indicated by the fitting line in the plot; c) Evolution of first principal stress at failure with the relative contact radius. The initiation of failure displays a transition from the center to equatorial belt with the increasing relative contact radius, as highlighted by the background color. SEM images show the typical morphologies before (left images) and after (right images) fracture emerges, initiated either from the center (images above) or equatorial belt (images below). The yellow arrow in the image below marks the crack. Scale bars are 1 μm and 500 nm for the images above and below, respectively.

the defect that serves as crack initiation size (pores or organic-rich sites). Except for the largest SPs, all others fail due to the crack initiated from the equator, as shown in Fig. 4(c). Indeed, the probability of a larger defect existing in SPs increases with the SP size (D).

The size-dependent elastic moduli of HT and non-HT SPs are shown in Fig. 3(e), and this relationship (E vs D) can be roughly described by a power-law function, as $E \propto D^{-0.76}$ for HT SPs and $E \propto D^{-0.30}$ for non-HT SPs. Substituting this into Eq. (20), the correlation between the critical fracture stress and SPs' diameter can be expressed as $\sigma_c \propto D^{-0.88}$ for HT SPs and $\sigma_c \propto D^{-0.65}$ for non-HT SPs. The fracture stress measured by compression tests for different SPs is plotted in Fig. 4(b), and its relationship with SPs' diameter (D) can be described as $\sigma_c \propto D^{-0.92}$ for HT SPs and $\sigma_c \propto D^{-0.54}$ for non-HT SPs. A good alignment with the prediction of Griffith theory is found for crosslinked (HT) SPs. The discrepancy in the case of non-crosslinked (non-HT) SPs can be ascribed to the limited data points and occurrence of plasticity (in non-HT 15/3.6 μm SPs) violating the assumptions of the theory.

4. Conclusions

Supercrystalline spherical particles (supraparticles – SPs) prepared by emulsion templated self-assembly have been compressed in situ in the SEM to investigate their mechanical response. Their size-dependent structure, deformation and fracture behavior are revealed. A transition from anti-Mackay (rhomb-icosidodecahedral) structure to single FCC is observed with increasing SP size. Small SPs fracture in a brittle manner, whereas larger ones exhibit minor plasticity before fracture. Loading cycles cause the stiffening of SPs due to the compaction of organic ligands. The size-dependent elastic modulus of SPs, i.e. the smaller, the stiffer, is attributed to the increasing significance of surface tension as the size of SPs decreases. A transition of failure initiation site, from SPs' center to equatorial belt is noted with reducing size of SPs, associated with the corresponding shift in the location of the peak first principal stress. The fracture stress shows a size-dependent trend, i.e. increasing for smaller SPs, and this size effect can be rationalized by Griffith theory. All SPs show remarkably high mechanical properties, especially those with crosslinking of the organic ligands. In terms of the impact of the addition of squalene, it is observed that there is no enhancement in deformability of the SPs, but, instead, an overall weaker material. The exploration of deformation and failure behavior of SPs, and specifically the size-dependent phenomena, provide valuable insights for the development of hierarchical ceramic-based functional materials that are also mechanically robust [26]. The mechanical characteristics of SCNCs can be customized to fulfil the requirements of the higher hierarchical levels, given their potential diversity in composition, size and shape. Ultimately, this paves the way towards the development of macroscopic, robust and functional nano-architected materials.

CRediT authorship contribution statement

Bor Büsra: Investigation, Data curation. **Plunkett Alexander:** Investigation, Data curation. **Schneider Gerold A.:** Supervision. **Lilleodden Erica:** Supervision. **Yan Cong:** Writing – original draft, Visualization, Formal analysis. **Giuntini Diletta:** Visualization, Supervision, Conceptualization.

Declaration of Competing Interest

The authors declare that they have no known competing financial interests or personal relationships that could have appeared to influence the work reported in this paper.

Acknowledgments

The authors gratefully acknowledge the financial support from the Deutsche Forschungsgemeinschaft (DFG, German Research Foundation) – project No. GI 1471/1–1 and 192346071-SFB 986. We gratefully acknowledge the support of Mohammadhadi Maghsoudi and Yijuan Wu during the in situ compression tests at the Helmholtz-Zentrum Hereon Geesthacht.

Appendix A. Supporting information

Supplementary data associated with this article can be found in the online version at doi:10.1016/j.jeurceramsoc.2025.117482.

References

[1] M.R. Begley, D.S. Gianola, T.R. Ray, Bridging functional nanocomposites to robust macroscale devices, Science 364 (2019) eaav4299, https://doi.org/10.1126/science.aav4299.
[2] E.V. Sturm, H. Cölfen, Mesocrystals: past, presence, future, Crystals 7 (2017) 207, https://doi.org/10.3390/cryst7070207.
[3] M.A. Boles, M. Engel, D.V. Talapin, Self-assembly of colloidal nanocrystals: from intricate structures to functional materials, Chem. Rev. 116 (2016) 11220–11289, https://doi.org/10.1021/acs.chemrev.6b00196.
[4] E. Tam, P. Podsiadlo, E. Shevchenko, D.F. Ogletree, M.P. Delplancke-Ogletree, P. D. Ashby, Mechanical properties of face-centered cubic supercrystals of nanocrystals, Nano Lett. 10 (2010) 2363–2367, https://doi.org/10.1021/nl1001313.
[5] A. Dreyer, A. Feld, A. Kornowski, E.D. Yilmaz, H. Noei, A. Meyer, T. Krekeler, C. Jiao, A. Stierle, V. Abetz, H. Weller, G.A. Schneider, Organically linked iron oxide nanoparticle supercrystals with exceptional isotropic mechanical properties, Nat. Mater. 15 (2016) 522–528, https://doi.org/10.1038/nmat4553.
[6] H.M. Lindsay, P.M. Chaikin, Elastic properties of colloidal crystals and glasses, J. Chem. Phys. 76 (1982) 3774–3781.
[7] X. Cao, E. Panizon, A. Vanossi, N. Manini, E. Tosatti, C. Bechinger, Pile-up transmission and reflection of topological defects at grain boundaries in colloidal crystals, Nat. Commun. 11 (2020) 3079, https://doi.org/10.1038/s41467-020-16870-w.
[8] S. Arai, H. Tanaka, Surface-assisted single-crystal formation of charged colloids, Nat. Phys. 13 (2017) 503–509, https://doi.org/10.1038/nphys4034.
[9] L. Bergström, E.V. Sturm, G. Salazar-Alvarez, H. Cölfen, Mesocrystals in biominerals and colloidal arrays, Acc. Chem. Res. 48 (2015) 1391–1402, https://doi.org/10.1021/ar500440b.
[10] M.P. Pileni, Nanocrystal self-assemblies: fabrication and collective properties, J. Phys. Chem. B 105 (2001) 3358–3371, https://doi.org/10.1021/jp0039520.
[11] T. Tachikawa, T. Majima, Metal oxide mesocrystals with tailored structures and properties for energy conversion and storage applications, NPG Asia Mater. 6 (2014) e100, https://doi.org/10.1038/am.2014.21.
[12] Z. Tang, N.A. Kotov, S. Magonov, B. Ozturk, Nanostructured artificial nacre, Nat. Mater. 2 (2003) 413–418, https://doi.org/10.1038/nmat906.
[13] F. Bouville, E. Maire, S. Meille, B. van de Moortèle, A.J. Stevenson, S. Deville, Strong, tough and stiff bioinspired ceramics from brittle constituents, Nat. Mater. 13 (2014) 508–514, https://doi.org/10.1038/nmat3915.
[14] U.G.K. Wegst, H. Bai, E. Saiz, A.P. Tomsia, R.O. Ritchie, Bioinspired structural materials, Nat. Mater. 14 (2015) 23–36, https://doi.org/10.1038/nmat4089.
[15] B. Bor, D. Giuntini, B. Domènech, M.V. Swain, G.A. Schneider, Nanoindentation-based study of the mechanical behavior of bulk supercrystalline ceramic-organic nanocomposites, J. Eur. Ceram. Soc. 39 (2019) 3247–3256, https://doi.org/10.1016/j.jeurceramsoc.2019.03.053.
[16] A. Plunkett, M. Kampferbeck, B. Bor, U. Sazama, T. Krekeler, L. Bekaert, H. Noei, D. Giuntini, M. Fröba, A. Stierle, H. Weller, T. Vossmeyer, G.A. Schneider, B. Domènech, Strengthening engineered nanocrystal three-dimensional superlattices via ligand conformation and reactivity, ACS Nano 16 (2022) 11692–11707, https://doi.org/10.1021/acsnano.2c01332.
[17] B. Bor, D. Giuntini, B. Domènech, A. Plunkett, M. Kampferbeck, T. Vossmeyer, H. Weller, I. Scheider, G.A. Schneider, Constitutive and fracture behavior of ultra-strong supercrystalline nanocomposites, Appl. Phys. Rev. 8 (2021) 031414, https://doi.org/10.1063/5.0056616.
[18] B. Bor, L. Heilmann, B. Domènech, M. Kampferbeck, T. Vossmeyer, H. Weller, G. A. Schneider, D. Giuntini, Mapping the mechanical properties of hierarchical supercrystalline ceramic-organic nanocomposites, Molecules 25 (2020) 4790, https://doi.org/10.3390/molecules25204790.
[19] C. Yan, B. Bor, A. Plunkett, B. Domènech, V. Maier-Kiener, D. Giuntini, Nanoindentation creep of supercrystalline nanocomposites, Mater. Des. 231 (2023) 112000, https://doi.org/10.1016/j.matdes.2023.112000.
[20] M.P. Pileni, Mechanical properties of supracrystals, EPL 119 (2017) 37002, https://doi.org/10.1209/0295-5075/119/37002.
[21] X.W. Gu, Mechanical properties of architected nanomaterials made from organic–inorganic nanocrystals, JOM 70 (2018) 2205–2217, https://doi.org/10.1007/s11837-018-3094-7.
[22] C. Yan, B. Bor, A. Plunkett, B. Domènech, G.A. Schneider, D. Giuntini, Nanoindentation of supercrystalline nanocomposites: linear relationship between elastic modulus and hardness, JOM 74 (2022) 2261–2276, https://doi.org/10.1007/s11837-022-05283-3.

[23] D. Giuntini, E. Torresani, K.T. Chan, M. Blankenburg, L. Saviot, B. Bor, B. Domènech, M. Shachar, M. Müller, E.A. Olevsky, J.E. Garay, G.A. Schneider, Iron oxide-based nanostructured ceramics with tailored magnetic and mechanical properties: development of mechanically robust, bulk superparamagnetic materials, Nanoscale Adv. 1 (2019) 3139–3150, https://doi.org/10.1039/c9na00222g.

[24] B. Domènech, A. Plunkett, M. Kampferbeck, M. Blankenburg, B. Bor, D. Giuntini, T. Krekeler, M. Wagstaffe, H. Noei, A. Stierle, M. Ritter, M. Müller, T. Vossmeyer, H. Weller, G.A. Schneider, Modulating the mechanical properties of supercrystalline nanocomposite materials via solvent-ligand interactions, Langmuir 35 (2019) 13893–13903, https://doi.org/10.1021/acs.langmuir.9b01938.

[25] C. Yan, D. Giuntini, Nanofatigue of supercrystalline nanocomposites, Int. J. Ceram. Eng. Sci. 6 (2024) e10199, https://doi.org/10.1002/ces2.10199.

[26] A. Plunkett, Kaan Temiz Chad Warren, Valea Wisniewski, Bodo Fiedler, Kaline P. Furlan, Javier Garay, Diletta Giuntini, Berta Domènech, Gerold A. Schneider, Bridging nanocrystals to robust, multifunctional, bulk materials through nature-inspired, Hierarchical Des., ChemRxiv (2022), https://doi.org/10.26434/chemrxiv-2022-mxtm4.

[27] P. Fratzl, R. Weinkamer, Nature's hierarchical materials, Prog. Mater. Sci. 52 (2007) 1263–1334.

[28] P. Stempflé, O. Pantalé, M. Rousseau, E. Lopez, X. Bourrat, Mechanical properties of the elemental nanocomponents of nacre structure, Mater. Sci. Eng. C. 30 (2010) 715–721, https://doi.org/10.1016/j.msec.2010.03.003.

[29] J. Koldehoff, M.V. Swain, G.A. Schneider, The geometrical structure of interfaces in dental enamel: a FIB-STEM investigation, Acta Biomater. 104 (2020) 17–27.

[30] A. Plunkett, C. Eldridge, G.A. Schneider, B. Domènech, Controlling the large-scale fabrication of supraparticles, J. Phys. Chem. B 124 (2020) 11263–11272, https://doi.org/10.1021/acs.jpcb.0c07306.

[31] J. Wang, C.F. Mbah, T. Przybilla, S. Englisch, E. Spiecker, M. Engel, N. Vogel, Free energy landscape of colloidal clusters in spherical confinement, ACS Nano 13 (2019) 9005–9015, https://doi.org/10.1021/acsnano.9b03039.

[32] J. Wang, C.F. Mbah, T. Przybilla, B. Apeleo Zubiri, E. Spiecker, M. Engel, N. Vogel, Magic number colloidal clusters as minimum free energy structures, Nat. Commun. 9 (2018) 5259, https://doi.org/10.1038/s41467-018-07600-4.

[33] S. Antonyuk, J. Tomas, S. Heinrich, L. Mörl, Breakage behaviour of spherical granulates by compression, Chem. Eng. Sci. 60 (2005) 4031–4044, https://doi.org/10.1016/j.ces.2005.02.038.

[34] J. Deneen, W.M. Mook, A. Minor, W.W. Gerberich, C.B. Carter, In situ deformation of silicon nanospheres, J. Mater. Sci. 41 (2006) 4477–4483, https://doi.org/10.1007/s10853-006-0085-9.

[35] M.M. Chaudhri, I.M. Hutchings, P.L. Makin, Plastic compression of spheres, Philos. Mag. A 49 (1984) 493–503, https://doi.org/10.1080/01418618408236551.

[36] E. Calvié, J. Réthoré, L. Joly-Pottuz, S. Meille, J. Chevalier, V. Garnier, Y. Jorand, C. Esnouf, T. Epicier, J.B. Quirk, K. Masenelli-Varlot, Mechanical behavior law of ceramic nanoparticles from transmission electron microscopy in situ nano-compression tests, Mater. Lett. 119 (2014) 107–110, https://doi.org/10.1016/j.matlet.2014.01.002.

[37] Z.L. Zhang, H. Kristiansen, J. Liu, A method for determining elastic properties of micron-sized polymer particles by using flat punch test, Comput. Mater. Sci. 39 (2007) 305–314, https://doi.org/10.1016/j.commatsci.2006.06.009.

[38] X. Li, B. Bhushan, A review of nanoindentation continuous stiffness measurement technique and its applications, Mater. Charact. 48 (2002) 11–36.

[39] W.M. Mook, J.D. Nowak, C.R. Perrey, C.B. Carter, R. Mukherjee, S.L. Girshick, P. H. McMurry, W.W. Gerberich, Compressive stress effects on nanoparticle modulus and fracture, Phys. Rev. B 75 (2007), https://doi.org/10.1103/PhysRevB.75.214112.

[40] D. Portnikov, H. Kalman, Determination of elastic properties of particles using single particle compression test, Powder Technol. 268 (2014) 244–252, https://doi.org/10.1016/j.powtec.2014.08.011.

[41] D. Guo, J. Li, G. Xie, Y. Wang, J. Luo, Elastic properties of polystyrene nanospheres evaluated with atomic force microscopy: size effect and error analysis, Langmuir 30 (2014) 7206–7212, https://doi.org/10.1021/la501485e.

[42] L. Kogut, I. Etsion, Elastic-plastic contact analysis of a sphere and a rigid flat, J. Appl. Mech. 69 (2002) 657–662, https://doi.org/10.1115/1.1490373.

[43] D.D. Stauffer, A. Beaber, A. Wagner, O. Ugurlu, J. Nowak, K. Andre Mkhoyan, S. Girshick, W. Gerberich, Strain-hardening in submicron silicon pillars and spheres, Acta Mater. 60 (2012) 2471–2478, https://doi.org/10.1016/j.actamat.2011.10.045.

[44] Y. Hiramatsu, Y. Oka, Determination of the tensile strength of rock by a compression test of an irregular test piece, Int. J. Rock. Mechan. Min. Sci. 3 (1966) 89–90.

[45] P.H. Shipway, I.M. Hutchings, Fracture of brittle spheres under compression and impact loading. I. Elastic stress distributions, Philos. Mag. A 67 (1993) 1389–1404, https://doi.org/10.1080/01418619308225362.

[46] P.H. Shipway, I.M. Hutchings, Fracture of brittle spheres under compression and impact loading. II. Results for lead-glass and sapphire spheres, Philos. Mag. A 67 (1993) 1405–1421, https://doi.org/10.1080/01418619308225363.

[47] V. Pejchal, G. Žagar, R. Charvet, C. Dénéréaz, A. Mortensen, Compression testing spherical particles for strength: theory of the meridian crack test and implementation for microscopic fused quartz, J. Mech. Phys. Solids 99 (2017) 70–92, https://doi.org/10.1016/j.jmps.2016.11.009.

[48] V. Pejchal, M. Fornabaio, G. Žagar, G. Riesen, R.G. Martin, J. Medřický, T. Chráska, A. Mortensen, Meridian crack test strength of plasma-sprayed amorphous and nanocrystalline ceramic microparticles, Acta Mater. 145 (2018) 278–289, https://doi.org/10.1016/j.actamat.2017.12.031.

[49] J. Wang, J. Schwenger, A. Ströbel, P. Feldner, P. Herre, S. Romeis, W. Peukert, B. Merle, N. Vogel, Mechanics of colloidal supraparticles under compression, Sci. Adv. 7 (2021) eabj0954, https://doi.org/10.1126/sciadv.abj0954.

[50] D. Giuntini, S. Zhao, T. Krekeler, M. Li, M. Blankenburg, B. Bor, G. Schaan, B. Domènech, M. Müller, I. Scheider, M. Ritter, G.A. Schneider, Defects and plasticity in ultrastrong supercrystalline nanocomposites, Sci. Adv. 7 (2021) eabb6063, https://doi.org/10.1126/sciadv.abb60.

[51] B. De Nijs, S. Dussi, F. Smallenburg, J.D. Meeldijk, D.J. Groenendijk, L. Filion, A. Imhof, A. Van Blaaderen, M. Dijkstra, Entropy-driven formation of large icosahedral colloidal clusters by spherical confinement, Nat. Mater. 14 (2015) 56–60, https://doi.org/10.1038/nmat4072.

[52] L.M. Prince, D.J. Microemulsion, L.Harding 6. Cebula, R.H. Ottewill, P.N. Pusey, Phase behaviour of concentrated suspensions of nearly hard colloidal spheres, Nature 320 (1986) 340–342.

[53] P.G. Bolhuis, D. Frenkel, S.-C. Mau, D.A. Huse, Entropy difference between crystalline phases, Nature 388 (1997) 235–236.

[54] A.L. Mackay, A dense non-crystallographic packing of equal spheres, Acta Crystallogr 15 (1962) 916–918.

[55] D. Tabor, The hardness of metals, Oxford university press, 2000, pp. 44–66.

[56] W.D. Callister, Materials science and engineering: an introduction, John Wiley & Sons, 2007, pp. 131–172.

[57] K.L. Johnson, Contact mechanics, Cambridge university press, 1987, pp. 84–106.

[58] D. Giuntini, A. Davydok, M. Blankenburg, B. Domènech, B. Bor, M. Li, I. Scheider, C. Krywka, M. Müller, G.A. Schneider, Deformation behavior of cross-linked supercrystalline nanocomposites: an in situ SAXS/WAXS study during uniaxial compression, Nano Lett. 21 (2021) 2891–2897, https://doi.org/10.1021/acs.nanolett.0c05041.

[59] C. Yan, E. Hirschmann, M.G.D. Geers, D. Giuntini, Free volume and nonlinear viscoelasticity in supercrystalline nanocomposites: a nanoindentation driven modelling analysis, Mater. Des. 252 (2025) 113784, https://doi.org/10.1016/j.matdes.2025.113784.

[60] J. Paul, S. Romeis, J. Tomas, W. Peukert, A review of models for single particle compression and their application to silica microspheres, Adv. Powder Technol. 25 (2014) 136–153, https://doi.org/10.1016/j.apt.2013.09.009.

[61] S. Cuenot, C. Frétigny, S. Demoustier-Champagne, B. Nysten, Surface tension effect on the mechanical properties of nanomaterials measured by atomic force microscopy, Phys. Rev. B 69 (2004) 165410, https://doi.org/10.1103/PhysRevB.69.165410.

[62] G.Y. Jing, H.L. Duan, X.M. Sun, Z.S. Zhang, J. Xu, Y.D. Li, J.X. Wang, D.P. Yu, Surface effects on elastic properties of silver nanowires: contact atomic-force microscopy, Phys. Rev. B 73 (2006) 235409, https://doi.org/10.1103/PhysRevB.73.235409.

[63] G. Žagar, V. Pejchal, M. Kissling, A. Mortensen, On the diametric compression strength test of brittle spherical particles, Eur. J. Mech. A/Solids 72 (2018) 148–154, https://doi.org/10.1016/j.euromechsol.2018.04.016.

[64] M. Li, I. Scheider, B. Bor, B. Domènech, G.A. Schneider, D. Giuntini, Ultra-thin and ultra-strong organic interphase in nanocomposites with supercrystalline particle arrangement: mechanical behavior identification via multiscale numerical modeling, Compos. Sci. Technol. 198 (2020) 108283, https://doi.org/10.1016/j.compscitech.2020.108283.

[65] A.A. Griffith VI., The phenomena of rupture and flow in solids, Philos. Trans. R. Soc. A 221 (1921) 163–198.